

**Microbially mediated kinetic sulfur isotope fractionation  
reactive transport modeling benchmark**

Cheng, Yiwei; Arora, Bhavna; Şengör, S. Sevinç; Druhan, Jennifer L.; Wanner, Christoph; van Breukelen, Boris M.; Steefel, Carl I.

**DOI**

[10.1007/s10596-020-09988-9](https://doi.org/10.1007/s10596-020-09988-9)

**Publication date**

2020

**Document Version**

Final published version

**Published in**

Computational Geosciences

**Citation (APA)**

Cheng, Y., Arora, B., Şengör, S. S., Druhan, J. L., Wanner, C., van Breukelen, B. M., & Steefel, C. I. (2020). Microbially mediated kinetic sulfur isotope fractionation: reactive transport modeling benchmark. *Computational Geosciences*, 25 (2021)(4), 1379-1391. <https://doi.org/10.1007/s10596-020-09988-9>

**Important note**

To cite this publication, please use the final published version (if applicable).  
Please check the document version above.

**Copyright**

Other than for strictly personal use, it is not permitted to download, forward or distribute the text or part of it, without the consent of the author(s) and/or copyright holder(s), unless the work is under an open content license such as Creative Commons.

**Takedown policy**

Please contact us and provide details if you believe this document breaches copyrights.  
We will remove access to the work immediately and investigate your claim.

***Green Open Access added to TU Delft Institutional Repository***

***'You share, we take care!' - Taverne project***

**<https://www.openaccess.nl/en/you-share-we-take-care>**

Otherwise as indicated in the copyright section: the publisher is the copyright holder of this work and the author uses the Dutch legislation to make this work public.



# Microbially mediated kinetic sulfur isotope fractionation: reactive transport modeling benchmark

Yiwei Cheng<sup>1</sup> · Bhavna Arora<sup>2</sup> · S. Sevinç Şengör<sup>3</sup> · Jennifer L. Druhan<sup>4</sup> · Christoph Wanner<sup>5</sup> · Boris M. van Breukelen<sup>6</sup> · Carl I. Steefel<sup>2</sup>

Received: 8 January 2019 / Accepted: 24 June 2020 / Published online: 28 August 2020  
© Springer Nature Switzerland AG 2020

## Abstract

Microbially mediated sulfate reduction is a ubiquitous process in many subsurface systems. Isotopic fractionation is characteristic of this anaerobic process, since sulfate-reducing bacteria (SRB) favor the reduction of the lighter sulfate isotopologue ( $S^{32}O_4^{2-}$ ) over the heavier isotopologue ( $S^{34}O_4^{2-}$ ). Detection of isotopic shifts has been utilized as a proxy for the onset of sulfate reduction in subsurface systems such as oil reservoirs and aquifers undergoing heavy metal and radionuclide bioremediation. Reactive transport modeling (RTM) of kinetic sulfur isotope fractionation has been applied to field and laboratory studies. We developed a benchmark problem set for the simulation of kinetic sulfur isotope fractionation during microbially mediated sulfate reduction. The benchmark problem set is comprised of three problem levels and is based on a large-scale laboratory column experimental study of organic carbon amended sulfate reduction in soils from a uranium-contaminated aquifer. Pertinent processes impacting sulfur isotopic composition such as microbial sulfate reduction and iron-sulfide reactions are included in the problem set. This benchmark also explores the different mathematical formulations in the representation of kinetic sulfur isotope fractionation as employed in the different RTMs. Participating RTM codes are the following: CrunchTope, TOUGHREACT, PHREEQC, and PHT3D. Across all problem levels, simulation results from all RTMs demonstrate reasonable agreement.

**Keywords** Reactive transport modeling · Benchmark · Microbial sulfate reduction · S isotopes · Kinetic isotope fractionation

---

**Electronic supplementary material** The online version of this article (<https://doi.org/10.1007/s10596-020-09988-9>) contains supplementary material, which is available to authorized users.

---

✉ Yiwei Cheng  
yiweicheng@lbl.gov

- <sup>1</sup> Climate and Ecosystem Sciences Division, Lawrence Berkeley National Laboratory, Berkeley, USA
- <sup>2</sup> Energy Geosciences Division, Lawrence Berkeley National Laboratory, Berkeley, USA
- <sup>3</sup> Now at Department of Environmental Engineering, Middle East Technical University, Ankara, Turkey
- <sup>4</sup> Department of Geology, University of Illinois Urbana-Champaign, Urbana, USA
- <sup>5</sup> Institute of Geological Sciences, University of Bern, Bern, Switzerland
- <sup>6</sup> Department of Water Management, Delft University of Technology, Delft, the Netherlands

## 1 Introduction

Dissimilatory sulfate reduction (DSR) occurs when sulfate-reducing microorganisms (SRM) oxidize organic matter anaerobically using sulfate as electron acceptor. Isotopic fractionation is typically characteristic of this anaerobic process, since sulfate-reducing bacteria (SRB) favor the reduction of the lighter sulfate isotopologue ( $^{32}SO_4^{2-}$ ) over the heavier isotopologue ( $^{34}SO_4^{2-}$ ) under the majority of environmental conditions. DSR occurs ubiquitously and plays an important role in sulfur cycling in natural terrestrial and marine sediments, causing wide range of  $\delta^{34}S$  signatures [1–3]. Fractionations in the  $^{34}S/^{32}S$  ratio have been extensively reported in marine, terrestrial, and subsurface environments and can vary widely. Sim et al. [3] reported values that range from < 10 to > 60‰. Recent pure culture experiments have demonstrated fractionation as large as 66‰ [3].

DSR is a key process in many subsurface applications such as remediation of uranium and acid mines. SRB populations are commonly limited by labile organic carbon substrate availability and are thus stimulated through the injection of organic carbon compounds in order to increase DSR rates, leading to

high rates of sulfate removal [4]. Organic carbon biostimulation experiments conducted in aquifers undergoing heavy metal and radionuclide remediation have pointed to a link between the onset of DSR and enhanced long-term stability of reduced uranium precipitates [5]. In offshore oil recovery operations, seawater is typically injected into the production reservoir to maintain pressure. Interaction of this sulfate-rich seawater with the organic carbon of the reservoir matrix creates favorable conditions for DSR, producing hydrogen sulfide, H<sub>2</sub>S. The toxic nature of this H<sub>2</sub>S poses health risks [6] to workers on site and compromises the integrity of metallic structure and pipeline equipment. Despite this range of environmental, infrastructure, and health effects, detection of DSR remains challenging, due to fluctuations in onsite background sulfate concentrations [7]. Further, effluent sulfide concentrations can react with iron minerals [8–10], thus masking their appearance in fluid samples. Breakthrough curves of sulfate  $\delta^{34}\text{S}$  have therefore been utilized as a more reliable and accurate proxy for the onset of DSR in subsurface systems.

In subsurface systems characterized by both chemical and physical complexity, the usage of traditional Rayleigh-type equations to model biological kinetic isotope fractionation has been shown to be inadequate [10–12]. Such simple distillation assumes that reactions are unidirectional, irreversible, and the only source of change to reactant concentrations [13], while reactions in soil systems are by and large, mediated by a broad range of factors including microorganisms via enzymatic reactions that follow Michaelis-Menten kinetics. Recent studies showed that the Rayleigh equation systematically underestimated the rate of biodegradation in subsurface systems undergoing enhanced remediation of organic pollutants [11, 14, 15]. Thus, reactive transport models (RTMs) are often necessary to quantitatively describe isotopic effects such as kinetic sulfur isotope fractionation. These simulations have been applied to both field and laboratory studies using a variety of mathematical formulations [10, 16–20].

Despite these studies and the availability of a large number of codes that essentially solve the same governing equations, benchmarking exercises are useful to document conceptual and numerical capabilities of models and identify needs for further improvement [21]. It is vital to note that benchmarking studies on isotopes are severely limited. For example, an earlier benchmark study of RTMs focused on simulating chromium (Cr) isotope fractionation during aqueous kinetic Cr(VI) reduction [22]. However, the simulation approaches employed by the RTMs in the Wanner et al. [22] benchmark were solely tested for first-order reaction kinetics and would not be applicable in simulating isotope fractionation associated with Monod-type rate laws. Similarly, the carbon isotope benchmark study by Druhan et al. [23] focused exclusively on a system where multiple aqueous species exist in tandem and require distinct equilibrium partitioning of the stable isotopes of carbon. In contrast, this particular benchmark helps provide

users' differences (or similarities) across codes based on capabilities for kinetic isotope fractionation, biomass growth, and different rate law formulations. Moreover, the coupled abiotic-biotic Fe-S cycling provides a new reference for future isotopic modeling studies.

The focus of this paper is thus to present a benchmark problem set for the simulation of kinetic sulfur isotope fractionation during DSR. Problems in this benchmark are derived from a well-characterized large column experiment [10]. Processes impacting sulfur isotopic composition such as microbial sulfate reduction and iron-sulfide reactions are included in the problem set. In addition, this benchmark also explores the different mathematical formulations in the representation of kinetic sulfur isotope fractionation as employed in the different RTMs. The multicomponent reactive transport codes used in this benchmark are the following: CrunchTope, TOUGHREACT, PHREEQC, and PHT3D. Capabilities and key features of the codes are described in Steefel et al. [24] and a quick summary is provided in Table 1.

## 2 Mathematical model description

### 2.1 Mass balance

All RTM software described herein utilize some form of a general reactive transport equation for a chemical species  $i$  as follows:

$$\frac{\partial(\phi S_L C_i)}{\partial t} = \nabla \cdot (\phi S_L D_i \nabla C_i) - \nabla \cdot (q C_i) - \sum_{j=1}^{N_j} \nu_{ij} R_j - \sum_{l=1}^{N_l} \nu_{il} R_l - \sum_{m=1}^{N_m} \nu_{im} R_m \quad (1)$$

where the term on the left hand side is the mass accumulation rate, the terms on the right hand side are diffusion/dispersion, advection terms, and reaction terms: aqueous phase reactions,  $R_j$ , mineral reactions,  $R_l$ , and gas reactions,  $R_m$ .  $N_x$  (where  $x = j, l, \text{ or } m$ ) represents the total number of reactions (aqueous, mineral, and gas phase respectively) that involve species  $i$ ;  $\nu_{ix}$  represents the stoichiometric coefficient of  $i$  associated with reaction  $x$ . Here  $\phi$  is porosity,  $S_L$  is liquid saturation,  $C_i$  is concentration (mol kgw<sup>-1</sup>),  $D$  is the diffusion/dispersion coefficient (m<sup>2</sup> s<sup>-1</sup>), and  $q$  is the Darcy flux (m s<sup>-1</sup>). The reaction network consists of aqueous speciation reactions, ion exchange, kinetic mineral dissolution and precipitation reactions, and microbially mediated redox reactions, which are described in the following subsections.

### 2.2 Aqueous equilibrium reactions and mineral dissolution and precipitation reactions

Aqueous speciation reactions between independent chemical components (i.e., primary species) and their derivatives (e.g.,

**Table 1** Reactive transport models used in this benchmark study and their capabilities. Adapted from Steefel et al. [24] and Arora et al. [42]

Reactive transport model	Capabilities
PHREEQC	<ul style="list-style-type: none"> <li>• 1D reactive multicomponent transport model</li> <li>• Transport reaction coupling based on sequential non-iterative approach (SNIA)</li> <li>• Discretization scheme–finite differences (mixing cells)</li> </ul>
TOUGHREACT (TR)	<ul style="list-style-type: none"> <li>• 3D reactive multicomponent transport model</li> <li>• SNIA</li> <li>• Integrated finite differences (finite volumes)</li> </ul>
CrunchTope (CT)	<ul style="list-style-type: none"> <li>• 3D reactive multicomponent transport model</li> <li>• SNIA (also global implicit approach)</li> <li>• Integrated finite differences (finite volumes)</li> </ul>
PHT3D	<ul style="list-style-type: none"> <li>• 3D reactive multicomponent transport model</li> <li>• Transport reaction coupling based on sequential non-iterative approach (SNIA)</li> <li>• Discretization scheme–finite differences (mixing cells)</li> </ul>

secondary species) are assumed to equilibrate instantaneously. Concentrations of secondary species are calculated as a function of the primary species using the law of mass action:

$$C_i = K_i^{-1} \gamma_i^{-1} \prod_{j=1}^{N_c} (\gamma_j C_j)^{v_{ij}} \tag{2}$$

where  $C$  is the concentration,  $K$  is the thermodynamic equilibrium constant,  $\gamma$  is the activity coefficient,  $v_{ij}$  is the stoichiometric coefficients in the reaction,  $N_c$  is the number of primary species, and subscripts  $j$  and  $i$  refer to the primary and secondary species respectively. In this benchmark, the following primary species are included in the model:  $H^+$ ,  $Fe^{2+}$ ,  $Fe^{3+}$ ,  $Na^+$ ,  $Ca^{2+}$ ,  $Mg^{2+}$ ,  $Cl^-$ ,  $^{32}SO_4^{2-}$ ,  $^{34}SO_4^{2-}$ ,  $H_2^{32}S_{(aq)}$ ,  $H_2^{34}S_{(aq)}$ ,  $CH_3COO^-$ ,  $CO_{2(aq)}$ ,  $O_{2(aq)}$ , and  $NH_4^+$ . Secondary species and corresponding reaction stoichiometry are listed in Table S1.

Mineral dissolution and precipitation rates are calculated following a transition state theory (TST) rate expression [25]:

$$R_l = k_m A_m \left[ 1 - \left( \frac{Q}{K_m} \right)^{m_2} \right]^{m_1} \tag{3}$$

where  $R_l$  is the reaction rate ( $mol\ kgw^{-1}\ s^{-1}$ ),  $k_m$  is the rate constant ( $mol\ m^{-2}\ s^{-1}$ ),  $A_m$  is the mineral reactive surface area ( $m^2_{mineral}\ kgw^{-1}$ ),  $Q$  refers to the ion activity product of a mineral dissolution/precipitation reaction, and  $K_m$  is the corresponding equilibrium constant. Exponents  $m_1$  and  $m_2$  are fitting parameters determined from experiments. A linear form to Eq. 3 is assumed, and the exponents  $m_1$  and  $m_2$  are set to 1. Table 2 shows the reaction stoichiometry of mineral reactions involved in these benchmark problems.

### 2.3 Representation of microbially-mediated reaction kinetics

The bioenergetics conceptual approach as developed by Rittman and McCarty [26] has been adopted to quantitatively

relate bacterial growth and energetics of redox reactions. In this framework, sulfate-reducing microorganisms (SRM, represented as  $C_5H_7O_2N$ ) catalyze the reaction between an electron donor (acetate in this case) and an electron acceptor (sulfate in this case) to derive energy for respiration, growth, and maintenance. A dual Monod equation is utilized to mathematically represent the coupled microbial sulfate reduction and acetate oxidation:

$$R_k = \mu[SRM] \frac{[eDonor]}{[eDonor] + K_{eDonor}} \frac{[eAcceptor]}{[eAcceptor] + K_{eAcceptor}} \tag{4}$$

where  $R_k$  ( $mol\ kgw^{-1}\ day^{-1}$ ) is the growth rate of the SRM,  $\mu$  ( $mol\ mol-C_5H_7O_2N^{-1}\ day^{-1}$ ) is the maximum specific growth rate, and  $K_e$  ( $mol\ kgw^{-1}$ ) is the half saturation constant of the electron donor/acceptor. The decay of biomass is modeled with a first-order decay model with a decay constant of  $0.00027\ day^{-1}$  following Druhan et al. [10].

### 2.4 Representation of sulfur isotope fractionation kinetics

Druhan et al. [10] explicitly represented the kinetics of the individual isotopologues of sulfur,  $^{32}SO_4^{2-}$ , and  $^{34}SO_4^{2-}$  through modification of the Monod rate law. Here we show this modification in terms of a single Monod expression concerning sulfate reduction, but it is equally applicable to a dual Monod expression as shown above (Eq. 4)

$$^{32}r = ^{32}\mu[SRM] \frac{[^{32}SO_4^{2-}]}{[^{32}SO_4^{2-}] + ^{32}K_s \left( 1 + \frac{[^{34}SO_4^{2-}]}{^{34}K_s} \right)} \tag{5a}$$

$$^{34}r = ^{34}\mu[SRM] \frac{[^{34}SO_4^{2-}]}{[^{34}SO_4^{2-}] + ^{34}K_s \left( 1 + \frac{[^{32}SO_4^{2-}]}{^{32}K_s} \right)} \tag{5b}$$

**Table 2** Mineral reactions and associated parameters for problem level 3

Stoichiometry	$k$ (mol/m <sup>2</sup> /s)
$CaCO_{3(s)} + H^+ \leftrightarrow Ca^{2+} + HCO_3^-$	7.9433E-5
$MgCO_{3(s)} + H^+ \leftrightarrow Mg^{2+} + HCO_3^-$	4.1687E-10
$Fe^{2+} + H^{32}S^- \leftrightarrow Fe^{32}S_{(am)} + H^+$	1.0E-6
$Fe^{2+} + H^{34}S^- \leftrightarrow Fe^{34}S_{(am)} + H^+$	1.0E-6
$2Fe^{2+} + H^+ + {}^{32}S_{(s)} \leftrightarrow 2Fe^{3+} + H^{32}S^-$	1.0E-3
$2Fe^{2+} + H^+ + {}^{34}S_{(s)} \leftrightarrow 2Fe^{3+} + H^{34}S^-$	1.0E-3
$Fe(OH)_{3(s)} + 3H^+ \leftrightarrow Fe^{3+} + 3H_2O$	3.715E-10

By assuming a common half saturation constant for both  ${}^{32}r$  and  ${}^{34}r$ , we arrive at the following simplified set of isotope-specific dual Monod rate laws that also incorporate a dependency on electron donor (acetate) concentration:

$${}^{32}r = {}^{32}\mu[SRM] \frac{[{}^{32}SO_4^{2-}]}{[SO_4^{2-}] + K_S^{SO_4}} \frac{[Ac]}{[Ac] + K_S^{Ac}} \quad (6a)$$

$${}^{34}r = {}^{34}\mu[SRM] \frac{[{}^{34}SO_4^{2-}]}{[SO_4^{2-}] + K_S^{SO_4}} \frac{[Ac]}{[Ac] + K_S^{Ac}} \quad (6b)$$

As a result, the kinetic fractionation factor ( $\alpha$ ) is simply a ratio of the rate constants as shown below:

$$\alpha = \frac{{}^{34}\mu}{{}^{32}\mu} \quad (7)$$

In this work, all RTMs utilize kinetic expressions as described by Eqs. 6 and 7 for all problem sets.

One of the goals of this paper is the comparison of the different mathematical formulations in the representation of kinetic sulfur isotope fractionation as employed in the different RTMs. At problem level 2, another mathematical algorithm used in van Breukelen et al. [20, 27] is incorporated in PHREEQC for comparison with the algorithm as utilized in Druhan et al. [10]. In this treatment, for each compound, the light and the heavy isotope species were defined to reflect the compound's fraction of total concentration for the light and heavy isotopes, respectively. In other words, the concentration of an isotope species is here taken to be equal to its fraction multiplied by the compound's total concentration. Reaction rates are then given as follows:

$${}^{32}r = R_k \cdot \left( \frac{[{}^{32}SO_4^{2-}]}{[SO_4^{2-}]} \right) \quad (8a)$$

$${}^{34}r = R_k \cdot \left( \frac{[{}^{34}SO_4^{2-}]}{[SO_4^{2-}]} \right) \cdot [\varepsilon + 1] \quad (8b)$$

where  ${}^{32}r$  and  ${}^{34}r$  are the rates of the light and heavy isotopes, respectively,  $R_k$  is the overall rate of sulfate reduction (Eq. 4), and  $\varepsilon$  is the kinetic isotope enrichment factor of the reaction step ( $\varepsilon = \alpha - 1$ ).

### 3 Benchmark problem setup

Problem sets in this work are adapted from a set of reactive transport modeling studies based on both column and field experiments of a well-established US Department of Energy research site: the Integrated Field Research Challenge (IFRC), located in Rifle, CO, USA [5, 28–33]. The Rifle site is a former uranium ore processing facility. Bioremediation of uranium in the Rifle aquifer has been demonstrated through the injection of excess labile organic carbon in the form of dissolved acetate. Specifically, acetate was injected into the subsurface over multiple experiments to stimulate both Fe(III) and  $SO_4^{2-}$  reducing microbes and mediate the reduction of soluble U(VI) to insoluble U(IV), effectively reducing U(VI) concentrations in the groundwater [5, 28, 29]. These field experiments coupled with reactive transport modeling studies [34–39] have yielded numerous insights pertaining to bioremediation of uranium and similar heavy metals and radionuclides in subsurface environments.

For the present benchmarking study, chemical and isotopic data used to constrain reaction rates, as simulated by the RTM, are taken from a large-scale laboratory column experimental study of organic carbon amended sulfate reduction in soils from the Rifle site [10, 39]. Druhan et al. [10] set up a large-scale (1 m in length) flow through column to replicate field conditions of acetate amended biostimulation experiments in Rifle. One of the goals of the study was to demonstrate incorporation of revised mathematical formulations for microbially mediated redox reactions which can accurately model kinetics of stable isotopes of sulfur (e.g., Eq. 7) over wide range of substrate availability. The mathematical formulation was originally incorporated and validated using the CrunchTope RTM software [24]. The column replicated patterns observed in the field [8]: including an initial period of time in which iron reduction was the dominant reduction process, after which, sulfate reduction became the principle source of acetate consumption (Fig. S1). The CrunchTope simulation was also able to accurately capture the observed enrichment in  $\delta^{34}S$  of both sulfate and sulfide, including both aqueous phase reactant and product pools as well as reduced sulfur minerals. The problem levels in this benchmark are derived from this well-characterized large column experiment. The benchmark is divided into three levels of incremental complexity with a sequential addition of reactive processes.



### 3.1 Microbial sulfate reduction along a 1D flow path (problem level 1)

The large-scale flow column is modeled as a 1D system of 1 m (height of column) discretized into 100 grid blocks of 0.01 m, with a porosity of 0.32. A constant flow rate of 12.7 cm day<sup>-1</sup>, similar to the experiments, was set in the model. The diffusion coefficient was assumed to be the same for aqueous chemical species and was set to 0.919 × 10<sup>-5</sup> cm<sup>2</sup> s<sup>-1</sup> and dispersivity is set at 4 cm [10]. Concentrations of the chemical species at the initial condition and influx boundary condition follow those from Druhan et al. [10] and are listed in Table 3. In this problem, only microbial sulfate reduction is simulated, and the concurrent reduction of Fe(III) by a separate population of microbial biomass is omitted for simplicity (see level 3). The terminal electron accepting process (TEAP), sulfate reduction, consists of two components: catabolic energy production and anabolic growth. This means that for each mole of electron donor (i.e., organic carbon substrate) utilized, a portion, *fs*, is used by the SRM for cell synthesis (anabolic) while the remaining fraction, *fe*, is used for energy production (catabolic) [26]. This catabolic component is the fraction of total acetate consumption that is coupled to the reduction of sulfate. For all simulations in this study, we assume a constant value of *fs* = 0.08 and *fe* = 0.92, such that 8% of the electrons provided by acetate oxidation are utilized for cell synthesis while the remaining 92% are used for energy production [10, 26]. The resulting stoichiometric equation is shown in Table 4.

Associated kinetic parameters for microbial sulfate reduction are also listed in Table 4.

### 3.2 Simulation of sulfate kinetic isotope fractionation along a 1D flow path (problem level 2a)

This problem builds on the processes and parameters described for problem level 1. The key difference is that at this level, kinetics of <sup>32</sup>SO<sub>4</sub><sup>2-</sup>, <sup>34</sup>SO<sub>4</sub><sup>2-</sup>, H<sup>32</sup>S<sup>-</sup>, and H<sup>34</sup>S<sup>-</sup> are explicitly represented (Table 3). The simulated kinetic fractionation factor is 0.987. Associated kinetic parameters for <sup>32</sup>SO<sub>4</sub><sup>2-</sup> and <sup>34</sup>SO<sub>4</sub><sup>2-</sup> reductions are listed in Table 4.

#### 3.2.1 Simulation of sulfate kinetic isotope fractionation under reactant limitation (problem level 2b)

This problem is similar in setting to problem level 2a. The only modification is that the initial and influent concentrations of <sup>32</sup>SO<sub>4</sub><sup>2-</sup> and <sup>34</sup>SO<sub>4</sub><sup>2-</sup> are reduced by one order of magnitude (lower than the half saturation constant of sulfate) (Table 3). The aim of this problem level is to verify the appropriate behavior of the kinetic isotope fractionation algorithm (Eq. 6) when the substrate concentration (sulfate in this case) is lower than the half saturation constant. The Monod-type rate expressions are of the functional form: *x*/(*x* + *K<sub>s</sub>*). Under conditions where the concentration of sulfate (or acetate) remains much higher than *K<sub>s</sub>*, the net rate is effectively subject to zero-order behavior. However, when the concentration of

**Table 3** Initial and influent concentration of the primary aqueous species in all levels

Primary species	Initial concentration (mmol/kg H <sub>2</sub> O)	Influent concentration (mmol/kg H <sub>2</sub> O)
pH	7.2	7.2
Fe <sup>2+</sup>	1.0E-08	1.0E-08
Fe <sup>3+</sup>	In equilibrium with iron hydroxide	In equilibrium with iron hydroxide
Na <sup>+</sup>	10.6	22.0
Ca <sup>2+</sup>	4.47	5.28
Mg <sup>2+</sup>	4.4	4.34
Cl <sup>-</sup>	3.00	3.00
HCO <sub>3</sub> <sup>-</sup>	8.66	3.25
Acetate	0.0	9.70
O <sub>2(aq)</sub>	15.6E-3	15.6E-3
NH <sub>4</sub> <sup>+</sup>	1.5	1.5
Br <sup>-</sup>	0.0	1.32
<sup>32</sup> SO <sub>4</sub> <sup>2-</sup> *^	8.80	8.80
<sup>34</sup> SO <sub>4</sub> <sup>2-</sup> *^^	3.9107925E-1	3.9107925E-1
H <sup>32</sup> S <sup>-</sup> **	1.0E-15	1.0E-15
H <sup>34</sup> S <sup>-</sup> **	4.44083904E-17	4.44083904E-17

\* Concentrations of <sup>32</sup>SO<sub>4</sub><sup>2-</sup> and <sup>34</sup>SO<sub>4</sub><sup>2-</sup> summed together in level 1

\*\* Concentrations of H<sup>32</sup>S<sup>-</sup> and H<sup>34</sup>S<sup>-</sup> summed together in level 1

^ Initial and influent concentrations of <sup>32</sup>SO<sub>4</sub><sup>2-</sup> are 0.88 mmol/kg H<sub>2</sub>O

^^ Initial and influent concentrations of <sup>34</sup>SO<sub>4</sub><sup>2-</sup> are 3.9107925E-2 mmol/kg H<sub>2</sub>O

**Table 4** Sulfate reduction terminal electron accepting process (TEAP) stoichiometry and associated parameters in levels 2 and 3. Iron reduction TEAP stoichiometry and associated parameters in Level 3

Microbe-mediated redox reactions	$\mu$	$K_{\text{TEAP}}$ (mol/kg H <sub>2</sub> O)	$K_{\text{AC}}$
(i) $0.115 \text{ }^{32}\text{SO}_4^{2-} + 0.125 \text{ CH}_3\text{CHOO}^- + 0.004 \text{ NH}_4^+ + 0.121 \text{ H}^+ \rightarrow 0.004 \text{ C}_5\text{H}_7\text{O}_2\text{N}_{\text{SRB}} + 0.23 \text{ HCO}_3^- + 0.115 \text{ H}_2\text{ }^{32}\text{S}_{(\text{aq})} + 0.012 \text{ H}_2\text{O}$	$3.21 \times 10^2 \text{ (mol/mol-C}_5\text{H}_7\text{O}_2\text{N/day)}^{++}$	$5.0 \times 10^{-3}$	$1.0 \times 10^{-4}$
(ii) $0.115 \text{ }^{34}\text{SO}_4^{2-} + 0.125 \text{ CH}_3\text{CHOO}^- + 0.004 \text{ NH}_4^+ + 0.121 \text{ H}^+ \rightarrow 0.004 \text{ C}_5\text{H}_7\text{O}_2\text{N}_{\text{SRB}} + 0.23 \text{ CO}_{2(\text{aq})} + 0.115 \text{ H}_2\text{ }^{34}\text{S}_{(\text{aq})} + 0.012 \text{ H}_2\text{O}$	$3.169212 \times 10^2 \text{ (mol/mol-C}_5\text{H}_7\text{O}_2\text{N/day)}^{++}$	$5.0 \times 10^{-3}$	$1.0 \times 10^{-4}$
(iii) $\text{Fe(III)(S)}^s + 0.208 \text{ CH}_3\text{CHOO}^- + 1.925 \text{ H}^+ + 0.033 \text{ NH}_4^+ \rightarrow 0.033 \text{ C}_5\text{H}_7\text{O}_2\text{N}_{\text{FeRB}} + 1.6 \text{ H}_2\text{O} + 0.25 \text{ HCO}_3^- + \text{Fe}^{2+}$	$2.7 \times 10^{-7} \text{ (mol/m}^3 \text{ cell/day)}^{++}$		$1.0 \times 10^{-5}$

<sup>++</sup> Units follow Druhan et al. (2014)

sulfate becomes much lower than the corresponding  $K_s$  value, the net rate approaches first-order behavior. The purpose of these isotope-specific rate law derivations is to allow smooth transition between the two end-member rate laws.

### 3.2.2 Comparison of kinetic isotope fractionation algorithms (problem level 2a and b)

In this level (2a and b), in addition to the formulation as shown in Druhan et al. [10] (Eq. 7a and b), the formulation as described in van Breukelen et al. [20, 27] (Eq. 8a and b) is incorporated in PHREEQC for comparison. Simulation results using this method are denoted as PHREEQC-alt in figures.

### 3.3 Simulation of sulfate kinetic isotope fractionation along a 1D flow path with microbial iron reduction and mineral dissolution/precipitation reactions (problem level 3)

This problem level adds mineral dissolution/precipitation reactions to level 2a. Seven minerals are included in this benchmark problem: calcite, magnesite, Fe(OH)<sub>3</sub>, Fe<sup>32</sup>S, Fe<sup>34</sup>S, <sup>32</sup>S<sup>0</sup>, and <sup>34</sup>S<sup>0</sup>. These minerals follow the mineral network described in Druhan et al. [10] and are considered to react under kinetic constraints and follow the TST rate law (eq. 3). <sup>32</sup>S<sup>0</sup> and <sup>34</sup>S<sup>0</sup> reaction rates are further dependent on the

activities of H<sub>2</sub><sup>32</sup>S<sub>(aq)</sub> and H<sub>2</sub><sup>34</sup>S<sub>(aq)</sub> respectively. The concurrent reduction of Fe(III) by a separate population of microbial biomass is also incorporated into this problem level. The mineral reactions used in this level are listed in Table 2. The resulting stoichiometric equation is shown in Table 4. Associated kinetic parameters for microbial iron and sulfate reduction are also listed in Table 4. Initial volume fraction and surface area of the minerals are listed in Table 5.

## 4 Results and discussion

### 4.1 Microbial sulfate reduction along a 1D flow path (problem level 1)

Simulation results show that the effluent pH of the system begins at 7.2 and increases asymptotically to 8 at the end of the experiment. Effluent sulfate concentrations remain near the initial and influent value of 9.2 mM for approximately the first 20 days of the experiment, a sign of insignificant microbial sulfate reduction. Beyond 20 days, the rate of microbial sulfate reduction began to increase, resulting in a corresponding decrease of both sulfate and acetate concentrations along the length of the column. Simulated effluent sulfate decreased to ~0 from 9.2 mM, while effluent acetate decreased to ~0 from initial values of 9.7 mM. At this problem

**Table 5** Initial conditions of mineral volume fraction for problem level 3

Mineral	Surface area	Volume fraction (m <sup>3</sup> m <sup>-3</sup> ) (mineral volume / total volume of solids)
Calcite	$1.04\text{E-}3 \text{ (cm}^2_{\text{mineral}} \text{ g}_{\text{mineral}}^{-1})$	0.069376
Magnesite	$1.00\text{E}6 \text{ (m}^2_{\text{mineral}} \text{ m}^3_{\text{mineral}}^{-1})$	1.47E-6
Fe <sup>32</sup> S <sub>(am)</sub>	$315 \text{ (cm}^2_{\text{mineral}} \text{ g}_{\text{mineral}}^{-1})$	0
Fe <sup>34</sup> S <sub>(am)</sub>	$315 \text{ (cm}^2_{\text{mineral}} \text{ g}_{\text{mineral}}^{-1})$	0
<sup>32</sup> S	$315 \text{ (cm}^2_{\text{mineral}} \text{ g}_{\text{mineral}}^{-1})$	0
<sup>34</sup> S	$315 \text{ (cm}^2_{\text{mineral}} \text{ g}_{\text{mineral}}^{-1})$	0
Fe(OH) <sub>3</sub>	$1.06\text{E}3 \text{ (m}^2_{\text{mineral}} \text{ m}^3_{\text{mineral}}^{-1})$	0.001382



level, simulated trends of pH and all primary species from all RTMs are in good agreement (Fig. 1).

### 4.2 Simulation of sulfate kinetic isotope fractionation along 1D flow path (problem levels 2a and 2b)

In problem level 2a, explicitly representation of  $^{32}\text{SO}_4^{2-}$ ,  $^{34}\text{SO}_4^{2-}$ ,  $\text{H}^{32}\text{S}^-$ , and  $\text{H}^{34}\text{S}^-$  allows us to calculate the sulfur isotope ratios of  $\text{SO}_4^{2-}$  and  $\text{HS}^-$ . These values are plotted and compared across all RTMs for the effluent fluid composition through time. Sulfur isotope ratios are reported in standard delta notation,  $\delta^{34}\text{S}$  (units of per mil, ‰), where  $R_{\text{sample}} = (^{34}\text{S}/^{32}\text{S})_{\text{sample}}$  and  $R_{\text{std}} = (^{34}\text{S}/^{32}\text{S})_{\text{std}}$ .  $R_{\text{std}}$  is the Canyon Diablo troilite standard (= 0.0441626):

$$\delta^{34}\text{S} = \left[ \left( \frac{R_{\text{sample}}}{R_{\text{std}}} \right) - 1 \times 1000 \right] \quad (9)$$

Effluent sulfate, sulfide, and acetate trends are similar to those in level 1. Specifically, the sum of the individual isotopologues (i.e.,  $^{32}\text{SO}_4^{2-} + ^{34}\text{SO}_4^{2-}$ ,  $\text{H}^{32}\text{S}^- + \text{H}^{34}\text{S}^-$ ) at level 2a is equivalent to  $\text{SO}_4^{2-}$  and  $\text{HS}^-$  curves at level 1 respectively.  $\delta^{34}\text{S}$  sulfate remained at the initial and up-gradient boundary value of + 6.3‰ for roughly the first 20 days of the experiment. Beyond 20 days,  $\delta^{34}\text{S}$  sulfate increased exponentially to a value of + 46‰ at the end of the experiment (day 43).  $\delta^{34}\text{S}$  of sulfide showed a similar trend, beginning at - 6.5‰ and ending at a value of + 4.9‰ on the last day of the

experiment. At this problem level, simulated trends of  $\delta^{34}\text{S}$  sulfate and sulfide from all RTMs match (Fig. 2).

Figure 3 shows the temporal trends of sulfate concentration and  $\delta^{34}\text{S}$  of sulfate at various locations along the column ( $x = 20, 40, 60,$  and  $80$  cm) for the complete duration of the 43-day acetate amendment. At any given point in time, sulfate concentration decreases with distance into the column. At day 43, sulfate concentrations are 1.9, 0.76, 0.45, and 0.34 mM at  $x = 20, 40, 60,$  and  $80$  cm respectively.  $\delta^{34}\text{S}$  of sulfate similarly enriches with distance into the column. At day 43,  $\delta^{34}\text{S}$  sulfate values are 22.92, 33.74, 40.61, and 44.47 at  $x = 20, 40, 60,$  and  $80$  cm respectively. Sulfate concentration at 20 cm is 1.9 mM, indicating that 80% of the total influent sulfate is removed in the first 20 cm of the column. Simulated spatial trends of sulfate concentration and  $\delta^{34}\text{S}$  of sulfate from all RTMs match (Fig. 3).

At problem level 2b, with the initial and influent sulfate concentration much lower than the half saturation constant, the decrease in concentration in the effluent through time was relatively minor, from 0.919 to 0.915 mM over the 43-day period. Sulfide concentration increased correspondingly from 0 to  $3.44 \times 10^{-3}$  mM. Such high concentrations of sulfide only occur as a result of the lack of solid phase precipitation included in this portion of the benchmark. In the same period of time,  $\delta^{34}\text{S}$  of sulfate increased from 6.3 to 6.36. At this problem level, simulated trends of  $\delta^{34}\text{S}$  sulfate and from all RTMs match (Fig. 4).

Fig. 1 Simulated temporal trends of effluent pH, sulfate, sulfide, and acetate concentrations in level 1

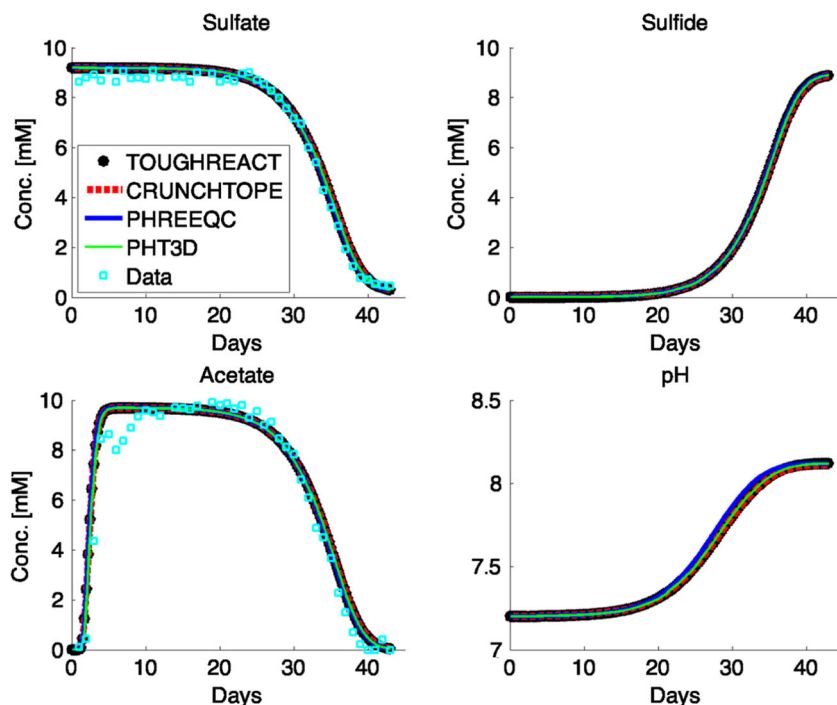
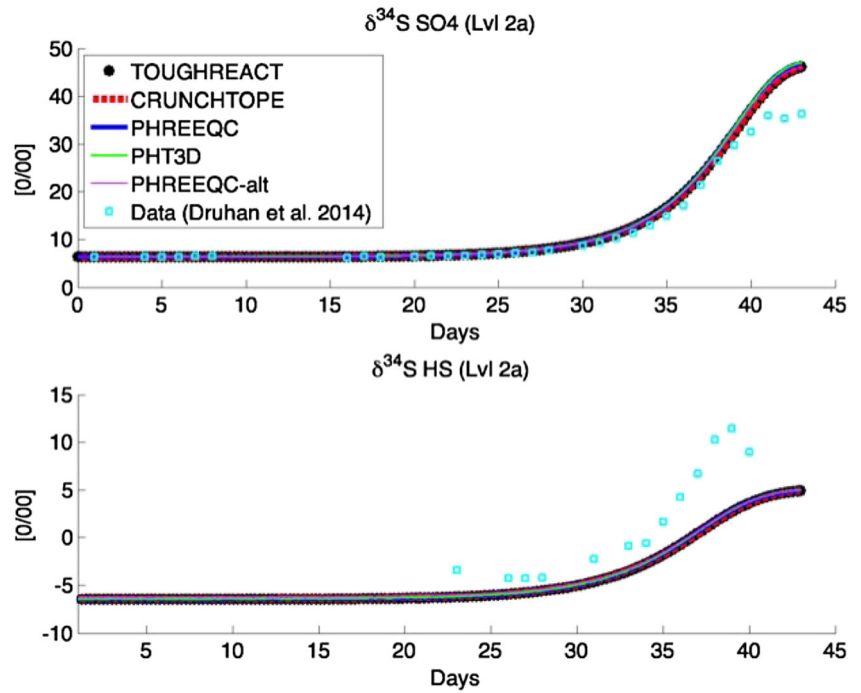


**Fig. 2** Simulated temporal trends of effluent  $\delta^{34}\text{S}$  sulfate (top) and sulfide (bottom) in level 2a



The results from level 2 show that the mathematical algorithms from van Breukelen et al. [20, 27] and Druhan et al. [10] yield similar behavior. Comparison of the mathematical expressions provides further support. Expanding Eq. 8b and substituting Eq. 7 and  $\varepsilon = \alpha - 1$ :

$$^{34}r = R_k \cdot \left( \frac{[^{34}\text{SO}_4^{2-}]}{[\text{SO}_4^{2-}]} \right) \cdot [\varepsilon + 1] = ^{32}\mu \cdot [\text{SRM}] \cdot \frac{[^{34}\text{SO}_4^{2-}]}{[\text{SO}_4^{2-}] + K_S^{\text{SO}_4^{2-}}} \cdot \frac{[\text{Ac}]}{[\text{Ac}] + K_S^{\text{Ac}}} \cdot \frac{^{34}\mu}{^{32}\mu} \tag{10}$$

**Fig. 3** Simulated temporal trends of sulfate and del34S sulfate in level 2a and  $x = 20$  (a), 40 (b), 60 (c), and 80 (d) cm at level 2a

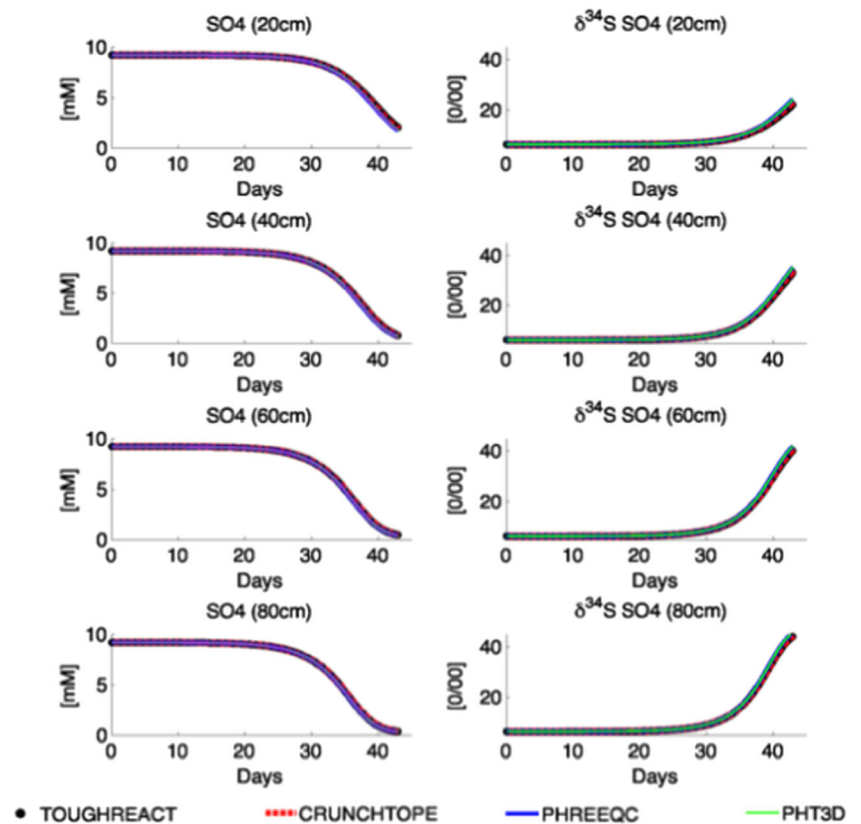
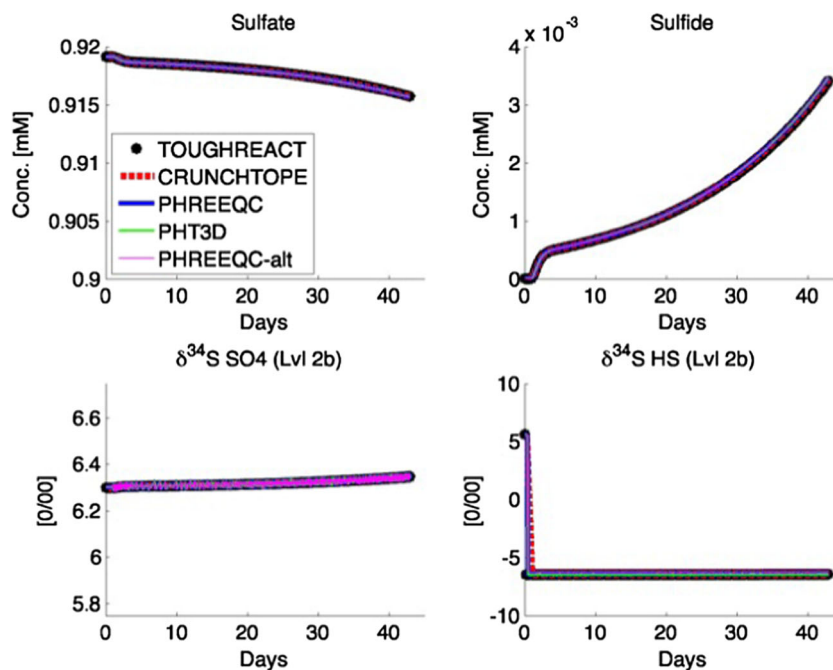


**Fig. 4** Simulated temporal trends of effluent sulfate, sulfide concentrations, and  $\delta^{34}\text{S}$  sulfate and sulfide in level 2b



We obtain the Eq. 6b under the simplifying assumption that the half saturation constants for the two isotopologues of sulfate are equivalent. These types of Monod formulations as utilized in van Breukelen et al. [20, 27] and Druhan et al. [10] coupled the two isotopologues to each other, thus enabling transition from zero-order to first-order reactions to occur (level 2a). The modified Monod formulation is distinct from the use of two fully independent Monod equations as utilized in earlier models, which may have limited these simulations to either zero-order or first-order conditions [16, 18].

It has been noted in van Breukelen et al. [20, 27] that a correction factor of the form:

$$\times \frac{1}{(A_H \times \alpha \times A_L)} \tag{11}$$

can be applied to each isotope/isotopologue reaction rate when the sum of the reaction rates of the individual isotopologues (e.g., Eq. 8) is lower than  $R_k$ , the overall rate.  $A_H$  and  $A_L$  are the abundances of the heavy and light isotope respectively. In this study, the correction factor was assumed to be  $\approx 1$ , permitting the derivation of equations as shown above. Further exploration of the impact of the correction factor is warranted. We reran simulation level 2a, this time with the inclusion of the correction factors. Results showed negligible differences between the simulation with and without the correction factor (Fig. S1). In addition, calculation of the correction factor at various time points of the simulation showed that the values  $\approx 1$ , justifying our assumption.

### 4.3 Simulation of sulfate kinetic isotope fractionation along a 1D flow path with microbial iron reduction and mineral dissolution/precipitation reactions (problem level 3)

Effluent sulfate, sulfide, acetate,  $\delta^{34}\text{S}$  sulfate, and  $\delta^{34}\text{S}$  sulfide trends are similar to those in level 2a (Fig. 5). Similar to the original study [9],  $\delta^{34}\text{S}$  sulfide trend was simulated through inclusion of a Fe-S precipitate as well as the formation of elemental sulfur. Effluent pH remained relatively stable at  $\sim 7.2$  throughout the experiment, indicating buffering as a result of water-rock interaction. Carbonate and  $\text{Fe}^{2+}$  concentrations showed increasing trends, while  $\text{Ca}^{2+}$  and  $\text{Mg}^{2+}$  concentrations showed decreasing trends.  $\text{Fe}^{3+}$  concentration increased rapidly within the first 2 days and thereafter slowly decreased to zero. Calcite volume fraction increased through time while magnesite content remained relatively constant throughout the duration of the experiment (Fig. 6).  $^{32}\text{S}^0$  ( $^{34}\text{S}^0$ ) minerals showed increasing trends in response to the increased production of sulfide. At this problem level, simulated trends of aqueous and mineral species of CrunchTope and TOUGHREACT matched reasonably well (Figs. 5 and 6).

In terms of process complexity, this problem level differs from the original Druhan et al. [10] simulation in the omission of a thermodynamic potential factor. This thermodynamic function,  $F_T$  limits the microbial-mediated reaction rates based on energetic constraints from the environment. In CrunchTope,  $F_T$  follows the Jin and Bethke [40] formulation, which represents

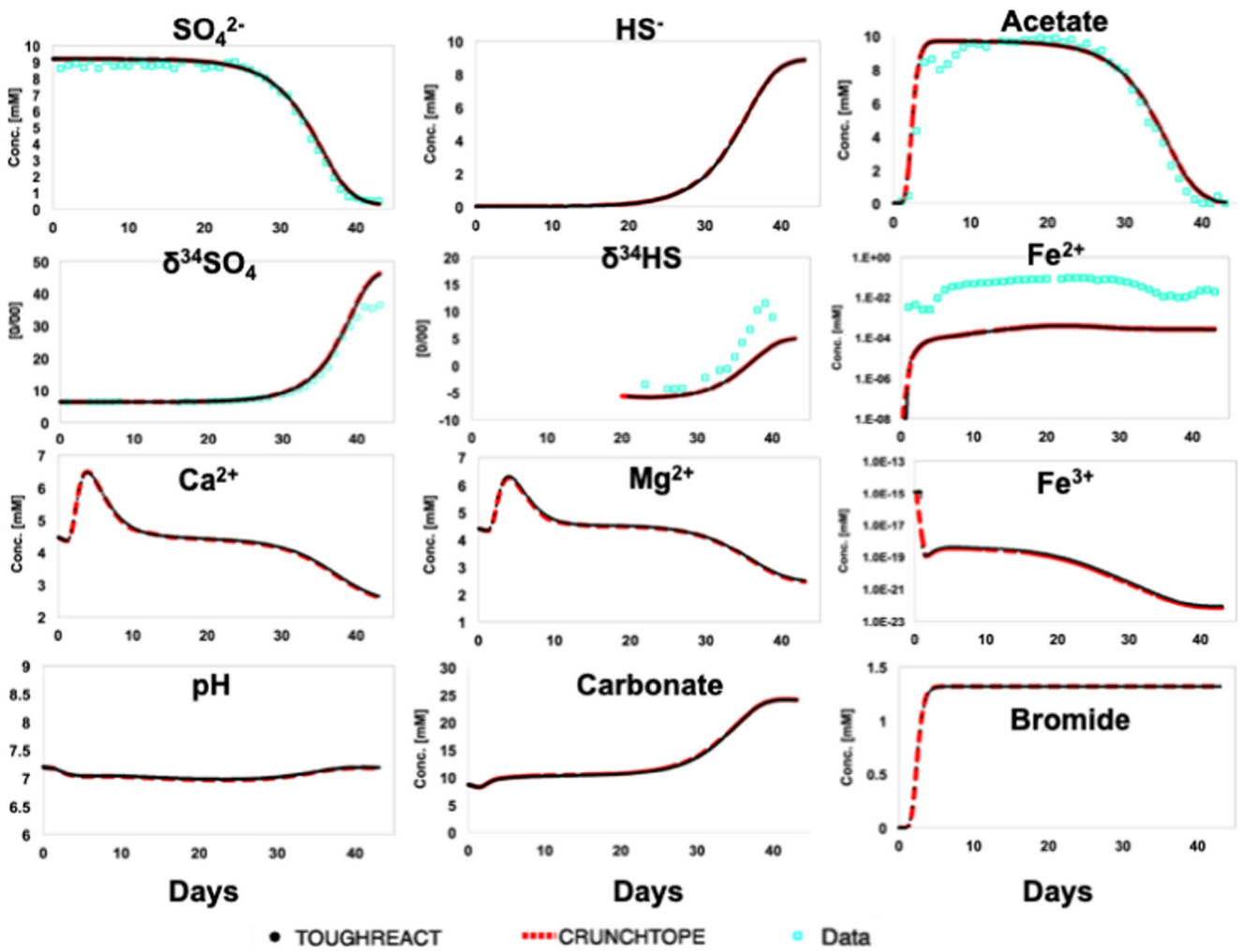
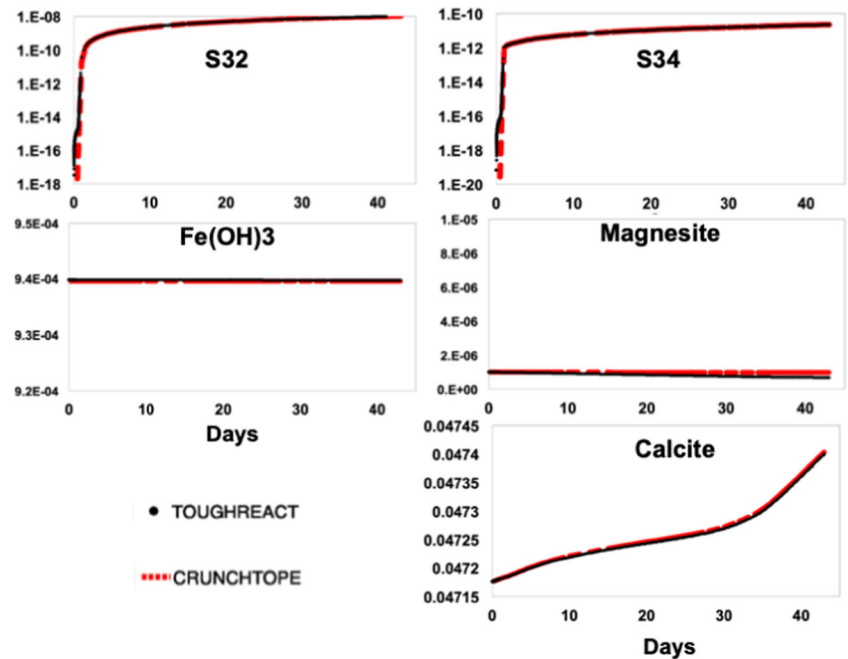


Fig. 5 Simulated temporal trends of effluent major aqueous chemical species and mineral species level 3

Fig. 6 Simulated temporal trends of mineral species level 3



$\Delta G_{\min}$ , minimum amount of energy microbial cells harvest for growth and maintenance, as the energetics of ATP synthesis by microorganisms, such that

$$F_T = 1 - e^{\left(\frac{\Delta G_r + m \Delta G_{ATP}}{\chi R T}\right)} \quad (12)$$

where  $\Delta G_r$  is the Gibbs free energy of a reaction per electron transferred,  $m$  is the number of moles of ATP produced per reaction,  $R$  is the gas constant ( $8.314 \text{ J mol}^{-1} \text{ K}^{-1}$ ),  $T$  is temperature (K), and  $\chi$  represents the average stoichiometric number for the reaction or the number of times the rate-determining step occurs in the overall reaction.  $\Delta G_{ATP}$  is the Gibbs free energy required to synthesize 1 mol of ATP, which is typically assumed to be  $\sim 60 \text{ kJ mol}^{-1}$  [41].  $m \Delta G_{ATP}$  is therefore the energy threshold required to synthesize ATP. While this thermodynamic function is coded in CrunchTope at the time of this writing, it is not yet available in TOUGHREACT, PHREEQC, and PHT3D. As such, we chose to omit this function in this level so as to allow comparison between CrunchTope and another RTM, TOUGHREACT.

## 5 Summary and conclusion

A benchmark problem set consisting of three problem levels was developed for the simulation of S isotope fractionation in a 1D flow through column. It was adapted from a large-scale laboratory column experimental study of organic carbon amended sulfate reduction in soils from a uranium-contaminated aquifer. This benchmark adds to the limited benchmarking studies on isotopes.

The first level considered the general conditions of flow and transport and basic sulfate reduction. The second level incorporated the kinetic fractionation of S isotopes under different reactant concentrations. The results were also calculated and compared using two different kinetic fractionation algorithms. In the final problem level, mineral precipitation/dissolution and coupled abiotic-biotic Fe-S cycling processes are systematically introduced to the system. This particular benchmark helps provide users' differences (or similarities) across codes based on capabilities for kinetic isotope fractionation, biomass growth, and different rate law formulations.

The benchmark problem set was solved with the following four well-established reactive transport modeling codes: CrunchTope, TOUGHREACT, PHREEQC, and PHT3D. For the first two problem levels, model-to-model comparisons showed excellent agreement, suggesting that for the tested geochemical processes (i.e., fractionation during microbial sulfate reduction) all of the tested codes are capable to accurately simulate the fate of individual S isotopes. In the final level, when mineral precipitation/dissolution and coupled abiotic-biotic Fe-S cycling processes are incorporated,

CrunchTope and TOUGHREACT simulations match. Future benchmarking efforts should expand to 2D (or 3D) problem levels that provide base case for validation, and cases involving heterogeneous redox and/or permeability distribution to tease apart the impacts of hydrodynamic dispersion and sulfate reduction on sulfur isotope fractionation.

**Acknowledgments** This work was supported as part of the Watershed Function Science Focus Area at Lawrence Berkeley National Laboratory funded by the U.S. Department of Energy, Office of Science, Biological and Environmental Research under Contract No. DE-AC02-05CH11231. This work was also supported in part by the Energy Biosciences Institute. The authors would like to thank the reviewers for their constructive comments.

This material is based upon work supported as part of the Energy Biosciences Institute and the Watershed Function Science Focus Area (SFA). The Watershed Function SFA at Lawrence Berkeley National Laboratory is funded by the U.S. Department of Energy, Office of Science, Biological and Environmental Research under Contract No. DE-AC02-05CH11231.

**Funding information** This material is based upon work supported as part of the Energy Biosciences Institute and the Watershed Function Science Focus Area (SFA).

## References

1. Canfield, D.E., Thamdrup, B., Fleischer, S.: Isotope fractionation and sulfur metabolism by pure and enrichment cultures of elemental sulfur-disproportionating bacteria. *Limnol. Oceanogr.* **43**(2), 253–264 (1998). <https://doi.org/10.4319/lo.1998.43.2.0253>
2. Canfield, D.E.: Isotope fractionation by natural populations of sulfate-reducing bacteria. *Geochim. Cosmochim. Acta.* **65**(7), 1117–1124 (2001). [https://doi.org/10.1016/S0016-7037\(00\)00584-6](https://doi.org/10.1016/S0016-7037(00)00584-6)
3. Sim, M.S., Bosak, T., Ono, S.: Large sulfur isotope fractionation does not require disproportionation. *Science.* **333**(6038), 74–77 (2011). <https://doi.org/10.1126/science.1205103>
4. Benner, S., Blowes, D., Ptacek, C., Mayer, K.: Rates of sulfate reduction and metal sulfide precipitation in a permeable reactive barrier. *Appl. Geochem.* **17**(3), 301–320 (2002). [https://doi.org/10.1016/S0883-2927\(01\)00084-1](https://doi.org/10.1016/S0883-2927(01)00084-1)
5. Williams, K.H., Long, P.E., Davis, J.A., Wilkins, M.J., N'Guessan, A.L., Steefel, C.I., Yang, L., Newcomer, D., Spane, F.A., Kerkhof, L.J., McGuinness, L., Dayvault, R., Lovley, D.R.: Acetate availability and its influence on sustainable bioremediation of uranium-contaminated groundwater. *Geomicrobiol J.* **28**(5–6), 519–539 (2011). <https://doi.org/10.1080/01490451.2010.520074>
6. Fuller, D.C., Suruda, A.J.: Occupationally related hydrogen sulfide deaths in the United States from 1984 to 1994. *J. Occup. Environ. Med.* **42**, 939–942 (2000). <https://doi.org/10.1097/00043764-200009000-00019>
7. Arora, B., Dwivedi, D., Hubbard, S.S., Steefel, C.I., Williams, K.H.: Identifying geochemical hot moments and their controls on a contaminated river floodplain system using wavelet and entropy approaches. *Environ. Model. Softw.* **85**, 27–41 (2016). <https://doi.org/10.1016/j.envsoft.2016.08.005>
8. Druhan, J.L., Steefel, C.I., Molins, S., Williams, K.H., Conrad, M.E., Depaolo, D.J.: Timing the onset of sulfate reduction over



- multiple subsurface acetate amendments by measurement and modeling of sulfur isotope fractionation. *Environ. Sci. Technol.* **46**(16), 8895–8902 (2012). <https://doi.org/10.1021/es302016p>
9. Hubbard, C.G., Cheng, Y., Engelbrekston, A., Druhan, J.L., Li, L., Ajo-Franklin, J.B., Coates, J.D., Conrad, M.E.: Isotopic insights into microbial sulfur cycling in oil reservoirs. *Front. Microbiol.* **5**(480), 1–12 (2014). <https://doi.org/10.3389/fmicb.2014.00480>
  10. Druhan, J.L., Steefel, C.I., Conrad, M.E., DePaolo, D.J.: A large column analog experiment of stable isotope variations during reactive transport: I. a comprehensive model of sulfur cycling and  $\delta^{34}\text{S}$  fractionation. *Geochim. Cosmochim. Acta.* **124**, 366–393 (2014). <https://doi.org/10.1016/j.gca.2013.08.037>
  11. Van Breukelen, B.M., Prommer, H.: Beyond the rayleigh equation: reactive transport modeling of isotope fractionation effects to improve quantification of biodegradation. *Environ. Sci. Technol.* **42**(7), 2457–2463 (2008). <https://doi.org/10.1021/es071981j>
  12. Maggi, F., Riley, W.J.: Transient competitive complexation in biological kinetic isotope fractionation explains nonsteady isotopic effects: theory and application to denitrification in soils. *J Geophys Res: Biogeophys.* **114**(G4), 1–13 (2009). <https://doi.org/10.1029/2008JG000878>
  13. Mariotti, A., Germon, J.C., Hubert, P., Kaiser, P., Letolle, R., Tardieux, A., Tardieux, P.: Experimental determination of nitrogen kinetic isotope fractionation: some principles; illustration for the denitrification and nitrification processes. *Plant Soil.* **62**(3), 413–430 (1981). <https://doi.org/10.1007/BF02374138>
  14. Abe, Y., Hunkeler, D.: Does the Rayleigh equation apply to evaluate field isotope data in contaminant hydrogeology? *Environ. Sci. Technol.* **40**(8), 1588–1596 (2006). <https://doi.org/10.1021/es051128p>
  15. Druhan, J.L., Maher, K.: The influence of mixing on stable isotope ratios in porous media: a revised Rayleigh model. *Water Resour. Res.* **53**(2), 1101–1124 (2017). <https://doi.org/10.1002/2016WR019666>
  16. Dale, A.W., Brüchert, V., Alperin, M., Regnier, P.: An integrated sulfur isotope model for Namibian shelf sediments. *Geochim. Cosmochim. Acta.* **73**(7), 1924–1944 (2009). <https://doi.org/10.1016/j.gca.2008.12.015>
  17. Gibson, B.D., Amos, R.T., Blowes, D.W.:  $^{34}\text{S}/^{32}\text{S}$  fractionation during sulfate reduction in groundwater treatment systems: reactive transport modeling. *Environ. Sci. Technol.* **45**(7), 2863–2870 (2011). <https://doi.org/10.1021/es1038276>
  18. Wehrmann, L.M., Arndt, S., März, C., Ferdelman, T.G., Brunner, B.: The evolution of early diagenetic signals in Bering Sea subseafloor sediments in response to varying organic carbon deposition over the last 4.3Ma. *Geochim. Cosmochim. Acta.* **109**, 175–196 (2013). <https://doi.org/10.1016/j.gca.2013.01.025>
  19. Cheng, Y., Hubbard, C.G., Li, L., Bouskill, N., Molins, S., Zheng, L., Sonnenthal, E., Conrad, M.E., Engelbrekston, A., Coates, J.D., Ajo-Franklin, J.B.: Reactive transport model of Sulfur cycling as impacted by perchlorate and nitrate treatments. *Environ. Sci. Technol.* **50**(13), 7010–7018 (2016). <https://doi.org/10.1021/acs.est.6b00081>
  20. Van Breukelen, B.M., Thouement, H.A.A., Stack, P.E., Vanderford, M., Philp, P., Kuder, T.: Modeling 3D-CSIA data: carbon, chlorine, and hydrogen isotope fractionation during reductive dechlorination of TCE to ethene. *J. Contam. Hydrol.* (2017). <https://doi.org/10.1016/j.jconhyd.2017.07.003>
  21. Dwivedi, D., Arora, B., Molins, S., Steefel, C.I.: Benchmarking reactive transport codes for subsurface environmental problems. *Groundwater Assessment, Modeling, and Management* (2016)
  22. Wanner, C., Druhan, J.L., Amos, R.T., Alt-Epping, P., Steefel, C.I.: Benchmarking the simulation of Cr isotope fractionation. *Comput. Geosci.* **19**(3), 497–521 (2015). <https://doi.org/10.1007/s10596-014-9436-9>
  23. Druhan, J.L., Guillon, S., Lincker, M., Arora, B.: Stable and radioactive carbon isotope partitioning in soils and saturated systems: a reactive transport modeling benchmark study. *Comput. Geosci.* **1–11** (2020). <https://doi.org/10.1007/s10596-020-09937-6>
  24. Steefel, C.I., Appelo, C.A.J., Arora, B., Jacques, D., Kalbacher, T., Kolditz, O., Lagneau, V., Lichtner, P.C., Mayer, K.U., Meeussen, J.C.L., Molins, S., Moulton, D., Shao, H., Šimůnek, J., Spycher, N., Yabusaki, S.B., Yeh, G.T.: Reactive transport codes for subsurface environmental simulation. *Comput. Geosci.* **19**, 445–478 (2015). <https://doi.org/10.1007/s10596-014-9443-x>
  25. Lasaga, A.C.: Chemical kinetics of water-rock interactions. *J Geophys Res: Solid Earth.* **89**(B6), 4009–4025 (1984). <https://doi.org/10.1029/JB089iB06p04009>
  26. Rittmann, B.E., McCarty, P.L., Rittman, B.E., McCarty, P.L.: *Environmental Biotechnology: Principles and Applications.* **1**, 10 (2010)
  27. Van Breukelen, B.M., Hunkeler, D., Volkering, F.: Quantification of sequential chlorinated ethene degradation by use of a reactive transport model incorporating isotope fractionation. *Environ. Sci. Technol.* **39**(11), 4189–4197 (2005). <https://doi.org/10.1021/es048973c>
  28. Anderson, R.T., et al.: Stimulating the in situ activity of *Geobacter* species to remove uranium from the groundwater of a uranium-contaminated aquifer. *Appl. Environ. Microbiol.* **69**(10), 5884–5891 (2003). <https://doi.org/10.1128/AEM.69.10.5884-5891.2003>
  29. Vrionis, H.A.e. a.: Microbiological and geochemical heterogeneity in an in situ uranium bioremediation field site. *Appl. Environ. Microbiol.* **71**(10), 6308–6318 (2005). <https://doi.org/10.1128/AEM.71.10.6308-6318.2005>
  30. Yabusaki, S.B., Fang, Y., Long, P.E., Resch, C.T., Peacock, A.D., Komlos, J., Jaffe, P.R., Morrison, S.J., Dayvault, R.D., White, D.C., Anderson, R.T.: Uranium removal from groundwater via in situ biostimulation: field-scale modeling of transport and biological processes. *J. Contam. Hydrol.* **93**(1–4), 216–235 (2007). <https://doi.org/10.1016/j.jconhyd.2007.02.005>
  31. Arora, B., Spycher, N.F., Steefel, C.I., Molins, S., Bill, M., Conrad, M.E., Dong, W., Faybishenko, B., Tokunaga, T.K., Wan, J., Williams, K.H., Yabusaki, S.B.: Influence of hydrological, biogeochemical and temperature transients on subsurface carbon fluxes in a flood plain environment. *Biogeochemistry.* **127**(2–3), 367–396 (2016). <https://doi.org/10.1007/s10533-016-0186-8>
  32. Dwivedi, D., Arora, B., Steefel, C.I., Dafflon, B., Versteeg, R.: Hot spots and hot moments of nitrogen in a riparian corridor. *Water Resour. Res.* **54**(1), 205–222 (2018). <https://doi.org/10.1002/2017WR022346>
  33. Yabusaki, S.B., Wilkins, M.J., Fang, Y., Williams, K.H., Arora, B., Bargar, J., Beller, H.R., Bouskill, N.J., Brodie, E.L., Christensen, J.N., Conrad, M.E., Danczak, R.E., King, E., Soltanian, M.R., Spycher, N.F., Steefel, C.I., Tokunaga, T.K., Versteeg, R., Waichler, S.R., Wainwright, H.M.: Water table dynamics and biogeochemical cycling in a shallow, variably-saturated floodplain. *Environ. Sci. Technol.* **51**(6), 3307–3317 (2017). <https://doi.org/10.1021/acs.est.6b04873>
  34. Fang, Y., Yabusaki, S.B., Morrison, S.J., Amonette, J.P., Long, P.E.: Multicomponent reactive transport modeling of uranium bioremediation field experiments. *Geochim. Cosmochim. Acta.* **73**, 6029–6051 (2009). <https://doi.org/10.1016/j.gca.2009.07.019>
  35. Li, L., Steefel, C.I., Williams, K.H., Wilkins, M.J., Hubbard, S.S.: Mineral transformation and biomass accumulation associated with uranium bioremediation at rifle, Colorado. *Environ. Sci. Technol.* **43**, 5429–5435 (2009). <https://doi.org/10.1021/es900016v>
  36. Yabusaki, S.B., Fang, Y., Williams, K.H., Murray, C.J., Ward, A.L., Dayvault, R.D., Waichler, S.R., Newcomer, D.R., Spang, F.A., Long, P.E.: Variably saturated flow and multicomponent biogeochemical reactive transport modeling of a uranium bioremediation field experiment. *J. Contam. Hydrol.* **126**(3–4), 271–290 (2011). <https://doi.org/10.1016/j.jconhyd.2011.09.002>



37. Bao, C., Wu, H., Li, L., Long, P.E., Newcomer, D., Williams, K.H.: Uranium bioreduction rates across scales: biogeochemical “hot moments” and “hot spots” during a biostimulation experiment at rifle, Colorado. *Environ Sci Technol.* **48**(17), 10116–10127 (2014). <https://doi.org/10.1021/es501060d>
38. Arora, B., Davis, J.A., Spycher, N.F., Dong, W., Wainwright, H.M.: Comparison of electrostatic and non-electrostatic models for U (VI) sorption on aquifer sediments. *Groundwater.* **56**(1), 73–86 (2018)
39. Druhan, J.L., Bill, M., Lim, H., Wu, C., Conrad, M.E., Williams, K.H., DePaolo, D.J., Brodie, E.L.: A large column analog experiment of stable isotope variations during reactive transport: II. Carbon mass balance, microbial community structure and predation. *Geochim. Cosmochim. Acta.* **124**(366–393), (2014). <https://doi.org/10.1016/j.gca.2013.08.036>
40. Jin, Q., Bethke, C.M.: Cellular energy conservation and the rate of microbial sulfate reduction. *Geology.* **37**(11), 1027–1030 (2009). <https://doi.org/10.1130/G30185A.1>
41. Thauer, R.K., Jungermann, K., Decker, K.: Energy conservation in chemotrophic anaerobic bacteria. *Bacteriol. Rev.* **41**, 100–180 (1977)
42. Arora, B., Şengör, S.S., Spycher, N.F., Steefel, C.I.: A reactive transport benchmark on heavy metal cycling in lake sediments. *Comput. Geosci.* **19**(3), 613–633 (2015)

**Publisher's note** Springer Nature remains neutral with regard to jurisdictional claims in published maps and institutional affiliations.